INTERNATIONAL JOURNAL OF CLIMATOLOGY
Int. J. Climatol. (2013)
Published online in Wiley Online Library
(wileyonlinelibrary.com) DOI: 10.1002/joc.3853

RMetS
Royal Meteorological Society

Air temperature distribution over Mongolia using dynamical downscaling and statistical correction

Bayasgalan Gerelchuluun and Joong-Bae Ahn*

Division of Earth Environmental System, Pusan National University, Busan, Korea

ABSTRACT: In this study, dynamical downscaling was performed using the Weather Research and Forecast (WRF) model to attain fine-resolution gridded meteorological information capable of reflecting Mongolia's complex topographical effect. Mongolia's sparse station network, with an average inter-station distance 107 km, is incapable of representing the spatial distribution of climate variables, such as temperature, over the country's complex topography. In order to reproduce fine-scale air temperature in Mongolia, the National Centers for Environmental Prediction/National Center for Atmospheric Research reanalysis II data with 6-h intervals from 1981 to 2010 were used as the initial and boundary conditions of the WRF model. A one-way nesting system was applied for two nested domains with horizontal grid spaces of 60 and 20 km. For correction of the systematic biases induced by dynamical downscaling, a statistical correction method was used for the downscaled results simulated by the WRF model. The bias was divided into two parts: the mean and the perturbation. The former was corrected by using a weighting function and a temperature inversion, and the latter by using the self-organizing maps method. In the former correction, the temperature inversion, characterized by an inverted lapse rate, in which temperature increases with increasing height in the lower atmosphere, was considered only when the temperature inversion occurred. According to our result, the domain-averaged Root Mean Square Difference of the model-simulated annual mean temperature was decreased from 3.7 °C to 2.1 °C after the statistical and temperature inversion corrections. On the basis of our study, we suggested that the area-averaged, fine-resolution, annual mean temperature of Mongolia was 1.1 °C (station mean temperature 0.5 °C). Our correction method improves not only spatial patterns with fine resolution but also the time-varying temperature variance over Mongolia.

KEY WORDS dynamical downscaling; statistical correction; temperature inversion

Received 17 January 2013; Revised 22 September 2013; Accepted 27 September 2013

1. Introduction

Mongolia has more than 130 sparsely located meteorological stations. This sparse station network limits the possibility of obtaining the quantity of the fine-resolution weather and climate information of Mongolia.

The general circulation model (GCM), focusing on the global scale with coarse horizontal resolution, can be used to produce and reproduce weather and climate information (Meehl, 1995). However, with the horizontal scale, regional and local details influenced by spatial heterogeneities in the regional physiography can be lost in the GCM simulation. GCMs are, therefore, inherently unable to represent local subgrid-scale features and dynamics, such as local topographical characteristics and processes. Nevertheless, various statistical downscaling techniques are available to convert GCM outputs into local variables, which are appropriate for applications since local meteorological conditions are largely related to large-scale meteorology. The most widely used statistical downscaling tools usually apply linear methods, such as local scaling, multiple linear regression, canonical correlation analysis and singular value decomposition (Conway *et al.*, 1996; Henrik *et al.*, 1999; Coulibaly *et al.*, 2005; Sun and Chen, 2012).

Dynamically sophisticated methods that convert GCM output into regional meteorological variables using reliable regional climate model (RCM) are usually referred to as dynamical downscaling techniques. The downscaling based on the RCM simulation with nesting system is used to attain relatively fine horizontal resolution information of the order of tens kilometres or less over the selected domain of interest (e.g., Gomboluudev *et al.*, 2005; Im *et al.*, 2008; Altangerel *et al.*, 2011).

Although RCM can provide weather and climate information on a fine-scale in the area of interest, the model result contains errors and biases related due to incompleteness of the current model and modelling technique, lack of understanding of the complex nature of the earth system (Lorenz, 1963), the uncertainties in initial conditions, model physics and parameterizations, etc.

Therefore, various statistical correction techniques based on Model Output Statistic (Wilks, 1995) are largely used to remove systematic and non-systematic biases in the model results using both linear (e.g., Ahn *et al.*, 2002; Wood *et al.*, 2004; Déqué *et al.*, 2007; Fischer and

* Correspondence to: J.-B. Ahn, Division of Earth Environmental System, Pusan National University, Busan, Korea. E-mail: jbahn@pusan.ac.kr

Schär, 2010; Amengual *et al.*, 2012) and nonlinear (e.g., Xu, 1999; Schoof and Pryor, 2001; Ahn *et al.*, 2012) methods.

Ahn *et al.* (2012) used dynamical downscaling and statistical correction to remove the systematic biases from simulated results by dividing them into mean and perturbation parts. A self-organizing map (SOM) was firstly used to correct the perturbation part of the temperature bias (Ahn *et al.*, 2012).

In this study, the distribution of monthly temperature in Mongolia was reconstructed using dynamical downscaling with a horizontal resolution of 20×20 km and a statistical correction method for the removal of systematic biases in the downscaled results by dividing them into mean and perturbation parts. The effect of temperature inversion frequently occurring over Mongolia during winter was also corrected using a temperature inversion correction method developed in this study.

In Section 3, we explain the data used and the study methods. Section 4 compares the observation and downscaled results with and without statistical correction. The discussions and conclusions are presented in Section 5.

2. Temperature inversion features in Mongolia

Under general atmospheric condition, air temperature decreases with increasing height in the lower troposphere. However, inversions are sometimes created due to several reasons such as radiative cooling at the lower layer, subsidence adiabatic heating at the upper layer, and advections of warm air over cooler air or of cool air under warmer air. In short, the main conditions for the inversion are largely governed by advection and/or radiative cooling. Outgoing radiation, especially during clear winter nights, cools the land surface, which in turn cools the lowermost surface layers, creating surface inversion of a few meters to a few kilometres thick. Topography can also play a role in creating a temperature inversion since it can sometimes cause cold air to flow down into valleys from mountain ranges. The cold air flowing down to the valley smuggles into the warmer air lifting it from the surface of the valley, thus creating the inversion. In Mongolia, the inversion is mainly created by the mechanism of the radiative cooling and the effect of mountains during winter (Erdensukh, 2008).

There are three major mountain ranges in Mongolia (Figure 1). Altai Mountains, the highest stretches across the western and southwestern regions of the country extended southeast from northwest direction. The Khangai Mountains, also lying in the same direction, occupy much of central and north-central Mongolia. The Khentei Mountains are located near the Russian border, to the northeast of Ulaanbaatar. A large part of eastern Mongolia is occupied by plains. The lowest area is a depression extending in a southwest-to-northeast direction. The depression extends from the Gobi Desert region in the south to the eastern frontier and contains six lakes bounded by the Altai in the west, and Khangai in the east and north, called the Great Lakes Depression (area (a) in Figure 1). Tes (area (b) in Figure 1) is a river in Northwestern Mongolia and southern Tuva in Russia. The river flows through Mongolia and Russia, returning to Mongolia before entering Uvs Lake (Figure 1) located in the northwest of Mongolia. The lake is the largest lake in the country. Selenge (area (c) in Figure 1), a major river in Mongolia, is located in the northern part of Mongolia originated northwest of the Khangai Mountains to Baikal Lake. Several rivers including Orkhon Tuul and Chuluut Eg merge into Selenge River.

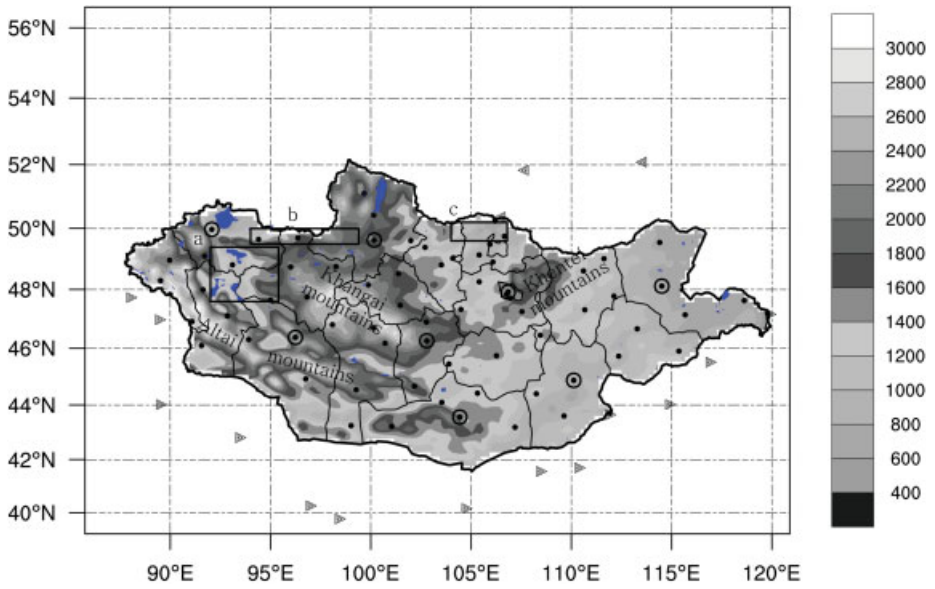

Figure 1. Location of meteorological and radiosonde stations. Black dots are meteorological stations in Mongolia. Westward (▶) and eastward (◀) directed triangles are Chinese and Russian stations respectively, and circled dots are radiosonde stations. Shading indicates elevation (unit: meter). Rectangular areas of (a), (b) and (c) correspond to Great Lakes Depression, Tes river basin and Selenge river basin, respectively.

Table 1. Monthly mean temperature inversion amount and depth observed at radiosonde stations.

WMO ID	Parameter	October	November	December	January	February	March
44277	Inversion (°C)		1.0	0.8	1.6	1.1	
	Depth (m)		863.5	833.0	814.0	807.4	
44288	Inversion (°C)						
	Depth (m)						
44373	Inversion (°C)		0.8	1.4	1.7	0.5	
	Depth (m)		533.6	521.1	507.5	500.6	
44231	Inversion (°C)	0.2	0.6	4.0	5.3	2.0	0.1
	Depth (m)	226.4	598.7	687.3	677.9	673.1	204.1
44259	Inversion (°C)	0.8	1.5	2.9	3.0	1.4	0.1
	Depth (m)	261.5	264.0	696.4	675.1	241.8	242.8
44212	Inversion (°C)			8.6	13.0	10.3	5.5
	Depth (m)			1879.0	2037.0	1865.0	897.1
44292	Inversion (°C)	0.0	0.4	2.9	3.2	1.3	
	Depth (m)	201.8	661.1	649.2	638.5	641.2	

The monthly mean temperature inversion observed from radiosonde stations is given in Table 1. It shows that the inversion took place from October to the following March in Mongolia, with no inversion in the other months. The largest amount of the inversion was 13.0 °C and the deepest depth was 2037 m, observed at Ulaangom station in January. The weakest inversion occurred at Arvaikheer station. The region of the deepest and largest inversion is surrounded by the major mountains, near the Uvs Lake.

In order to compare the observed inversion with the simulated results, vertical profiles of monthly mean winter temperature at Ulaangom and Arvaikheer stations where the deepest and weakest inversions were observed, respectively, are shown in Figures 2 and 3. In both temperature profiles, the observed and simulated profiles show temperature inversion during winter but the amount of the inversion differs near surface. The temperature inversion simulated by Weather Research and Forecast (WRF) is weaker than the observation. On the other hand, as shown in Figures 2 and 3, there are no inversions throughout the summer and WRF simulates the vertical profile of temperature reasonably well, as in the observation.

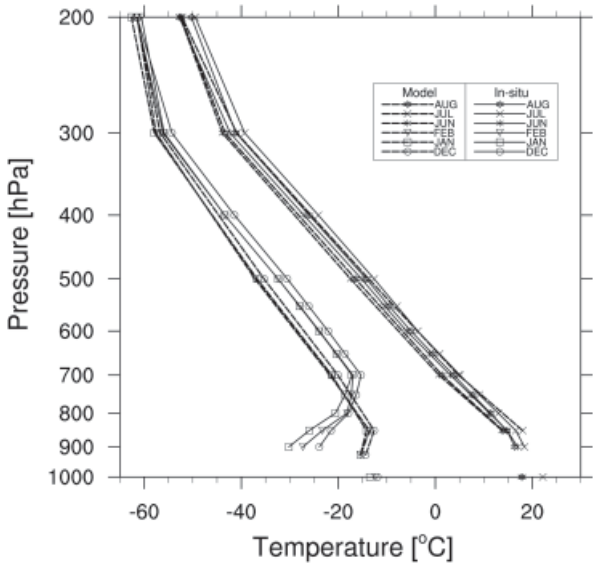

Figure 2. Monthly mean temperature profile in winter and summer, averaged over 1981–2010. Solid line is observation at Ulaangom station (WMO ID 44212). Dashed line indicates simulated temperature nearest to the station.

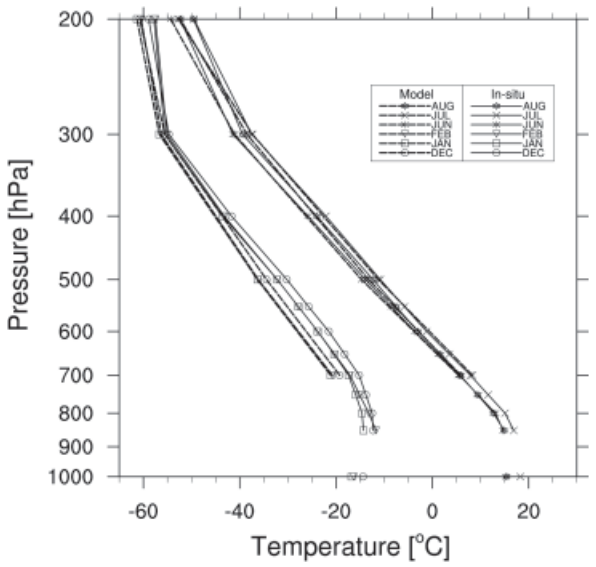

Figure 3. Monthly mean temperature profile in winter and summer, averaged over 1981–2010. Solid line is observation at Arvaikheer station (WMO ID 44288). Dashed line indicates simulated temperature nearest to the station.

The distribution of monthly temperature inversion over Mongolia from Erdenesukh (2008) was regridded, as shown in Figure 4. The largest temperature inversion occurred within the Great Lakes Depression located in between the Altai and Khangai mountain ranges, along the Tes and Selenge river basins. According to the inversion pattern, a relatively large inversion occurs along the Tes river valley in November but a weaker inversion occurs in the Great Lakes Depression due to effect of the lakes. After the lakes are frozen, the deepest inversion in the Great Lakes Depression is maintained until it decays in March. Moreover, as shown

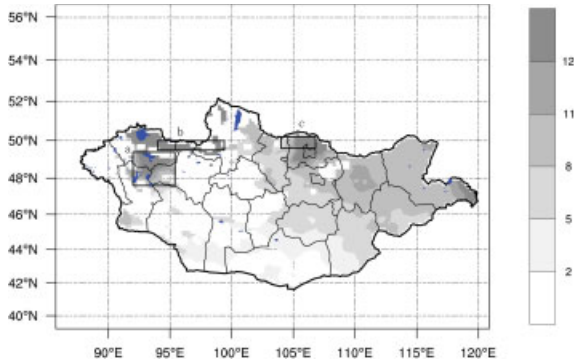

Figure 4. Monthly mean temperature inversion pattern in January from Erdenesukh (2008), which is regridded for the domain (Unit: °C). Rectangular areas of (a), (b) and (c) correspond to Great Lakes Depression, Tes river basin and Selenge river basin, respectively.

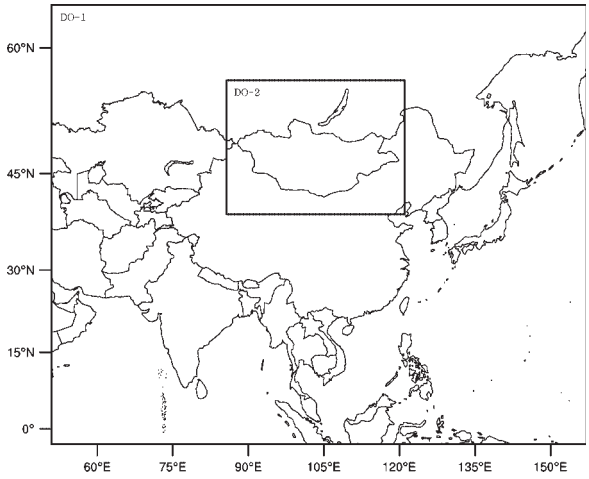

Figure 5. The first and second nested domains for dynamical downscaling with a horizontal resolution of 60×60 km, and 20×20 km, respectively.

in Figure 4, temperature inversion can occur in the other regions of Mongolia except the high mountain areas. In this study, the inversion distribution made by Erdensukh (2008), referred to as 'inversion correction', was used for a surface air temperature correction.

3. Data and method

3.1. Data

The National Centers for Environmental Prediction/National Center for Atmospheric Research (NCEP/NCAR) reanalysis II on a 2.5×2.5 grid from 1981 to 2010 was used to generate the initial and boundary conditions of the WRF model simulation.

The first nested domain for dynamical downscaling extended from 2°S to 67°N and from 51°E to 157°E with a horizontal resolution of 60×60 kilometre, and the second domain covered from 85°E to 121°E and from 39°N to 57°N with a horizontal resolution of 20×20 km (Figure 5). The second nested domain containing Mongolia was the analysis domain.

Data from 70 surface *in situ* and seven radiosonde observational stations (Figure 1) within the domain, provided by the National Agency for Meteorology, Hydrology and Environment Monitoring of Mongolia, were analyzed for the period 1981–2010. The locations of the observational station with their elevation are also shown in the figure. The topography clearly shows the complex spatial heterogeneities in the regional physiography. The mean distance between the stations is about 107.1 km and the mean elevation of the *in situ* observational sites is 1348 m (Table 2). The basic statistics regarding the station and model distances and elevations are listed in Table 2. The surface air temperature data from China and Russia located near the border of Mongolia were also used for statistical correction.

3.2. Dynamical downscaling

In order to relate the large-scale weather pattern to the regional scale based on physics, dynamical downscaling is necessary. RCMs are the ultimate useful tool for the informative downscaling approach. The WRF model used as RCM in this study was designed to be a flexible, state-of-the–art atmospheric simulation system.

Table 2. General distance and height from observation sites and model grid system.

	Distance (km)			Height (m)		
	Mean	Maximum	Minimum	Mean	Maximum	Minimum
Station	107.1	228.6	10.8	1348	2255	630
Model	20.0	20.0	20.0	1491	3109	537

In order to reproduce the fine-scale air temperature in Mongolia, dynamical downscaling was performed using the WRF model with the initial and boundary conditions from the NCEP/NCAR reanalysis II data with 6-h intervals from 1981 to 2010. The integration was restarted each month of each year and the 3 days prior to the first day of each month were assigned as the spin-up period for each simulation and removed from the analysis. One-way nesting system was applied, having two nested domains with a horizontal grid space of 60 and 20 km. The physical options for the WRF simulation include the microphysics WSM 6-class by Hong and Lim (2006), Rapid radiation transfer model long-wave radiation scheme by Mlawer *et al.* (1997), Dudhia short-wave radiation scheme by Dudhia (1989), Noah land surface model by Ek *et al.* (2003), Kain-Fritsch cumulus parameterization scheme by Kain (2004) and Yonsei University boundary layer scheme by Hong *et al.* (2006). In addition, the model configurations are given in Table 3. USGS 24-category land use categories (Table 4) were ingested into the Noah land surface model in WRF.

3.3. Statistical correction

Although WRF can provide information on various aspects of the weather and climate in the area of interest, the model results contain a certain amount of bias and

Table 3. Configuration of the WRF model with one-way nesting system.

Model configuration	WRFV3 description	
Dynamic core	ARW (Advanced Research WRF)	
Horizontal coordinate	Arakawa C grids	
Horizontal resolution	Domain 1	60×60 km
	Domain 2	20×20 km
Vertical coordinate	Mass-based following eta	
Vertical resolution	Domain 1, 2	28 levels (top pressure-50 hPa)
Physical scheme	Microphysics scheme	WSM 6-class graupel
	Cumulus parameterization	Kain-Fritsch
	Planetary boundary scheme	YSU
	Land surface model	Noah land surface model
	Short-wave radiation scheme	Dudhia scheme
	Long-wave radiation scheme	RRTM radiation

Table 4. USGS 24-category land use categories in WRF.

Land use category	Land use description
1	Urban and Built-Up Land
2	Dryland Cropland and Pasture
3	Irrigated Cropland and Pasture
4	Mixed Dryland/Irrigated Cropland and Pasture
5	Cropland/Grassland Mosaic
6	Cropland/Woodland Mosaic
7	Grassland
8	Shrubland
9	Mixed Shrubland/Grassland
10	Savanna
11	Deciduous Broadleaf Forest
12	Deciduous Needleleaf Forest
13	Evergreen Broadleaf
14	Evergreen Needleleaf
15	Mixed Forest
16	Water Bodies
17	Herbaceous Wetland
18	Wooden Wetland
19	Barren or Sparsely Vegetated
20	Herbaceous Tundra
21	Wooded Tundra
22	Mixed Tundra
23	Bare Ground Tundra
24	Snow or Ice

errors. In order to reduce these systematic biases, a method similar to that developed by Ahn *et al.* (2012) was used in this work.

Systematic biases were divided into two components, mean and perturbation parts that were statistically corrected by different methods independently.

For the statistical correction, gridded observation (A_o, the same horizontal resolution as the model) by objective analysis (Cressman, 1960) and the model output (A_m), which are divided into two parts, are expressed as follows:

$$A_o = \overline{A}_o + A_o^{'} \tag{1}$$

$$A_m = \overline{A}_m + A_m^{'} \tag{2}$$

where ($\overline{\ }$) and ($'$) represent the mean and perturbation parts, respectively, in each of the 156×117 grid points. The monthly mean temperature for each month in a span of 1981–2010 and the perturbation part in each month of every year in the span were calculated in both the observation and the model.

The mean bias corrected value $\left(\overline{C}_m\right)$ is expressed as shown by Ahn *et al.* (2012),

$$\overline{C}_m = (1 - W) \times \frac{\overline{A}_{m1} + \overline{A}_{m2}}{2} + W \times \overline{A}_{m2} \tag{3}$$

$$W = e^{-\left\{\left(\frac{h-981}{h_\sigma}\right)^2/4\right\}} \tag{4}$$

where $\overline{A}_{m1} = \overline{A}_m + \overline{A}_d$, $\overline{A}_{m2} = \overline{A}_m + (a_o - a_m)$ calculated at each grid 156×117 in the domain, and subscripts o and m denote the observation and model output, respectively. $\overline{A}_d$ is the difference in the mean parts of the observation and model. The mean values averaged over the domain (Figure 1) from the mean parts of the model output and gridded observation by the objective analysis (Cressman, 1960) were denoted as a_m and a_o, respectively. The simple objective interpolation method cannot properly represent the effect of elevation. Moreover, to preserve the change of temperature caused by landform more accurately in the mean values of a_m and a_o, W is expressed as a function of height, and the Gaussian function is used for W. In addition, h is the height from sea level and h_σ is the standard deviation of the height throughout all of Mongolia. The mean correction consists of the two terms expressed in Equation (3): the first expresses the values of monthly mean temperature and the second provides information of detailed topography on the temperature pattern. Detailed explanation for the method is described in Ahn *et al.* (2012).

In the cold season, as described in Equation (4), temperature inversion prevails in Mongolia. In case of temperature inversion, temperature is a function of height as follows (Erdenesukh, 2008):

$$T(\eta) = T_o - \gamma\eta \tag{5}$$

where γ is the lapse rate for air, η the height in inversion layer, and T_o the observed surface temperature at the grid points. Based on Equation (5), Erdenesukh (2008) expressed $T(\eta) = f(T_o, \gamma, \eta)$ using multiple linear regression. According to the inversion features in Mongolia, Equation (5) remains valid throughout the whole cold season according to the monthly vertical mean temperature distribution. In case of the inversion, Equation (3) reduced as follows:

$$\overline{C}_m = (1 - W) \times \frac{\overline{A}_{m1} + \overline{A}_{m2}}{2} + \Delta T \tag{6}$$

where $\Delta T = T(\eta) - T_o$, $T(\eta)$ from Erdenesukh (2008).

In order to embed the inversion into the temperature pattern, the amount of temperature inversion was used in the correction as in Equation (6) instead of the second term of Equation (3).

For the perturbation correction (C'), SOM, a kind of artificial neural network (ANN) was used. Several studies that focused on the temperature correction produced by RCM suggested that a nonlinear statistic method shows better performance than a linear statistic method (Xu, 1999; Schoof and Pryor, 2001; Ahn *et al.*, 2012). Especially, Ahn *et al.* (2012) concluded that variation would be highly affected by SOM applied to perturbation values.

SOM can be roughly divided into three categories, each based on a different philosophy (Kohonen, 1990): feedforward networks, feedback networks and self-organizing. Feedforward networks transform sets of input layers into sets of output layers. In other words, according to Kohonen's rule, the similarity between created arbitrary weight (W_i) and input layer (A_i) is calculated using Euclidian distance (Ahn *et al.*, 2012). In this step, the smallest value is called the 'winner neuron'. And then, winner neuron gets an opportunity to be trained as following:

$$W_i\,(t+1) = W_i\,(t) + B\,(A_i - W_i\,(t)) \qquad (7)$$

Here, the learning rate (B) controls when the winner neuron's weight calculated by Euclidian distance is updated. A low learning rate has the disadvantage of a slow training speed but the advantage of high accuracy, and vice versa in the case of a high learning rate. In the third category, neighbouring cells in a neural network compete in their activities by means of mutual lateral interactions, and develop adaptively into specific detectors of different signal pattern. This is called competitive and unsupervised method, or SOM. In other words, the neurons within the neighbourhood radius of the winner neuron, so called 'resemble neurons', are adjusted using a Gaussian function (Ahn *et al.*, 2012).

In this work, the perturbation of a model (A'_m) with 156×117 grids and the perturbation of observation (A'_o) were used as input layers, the initial learning rate was assigned as 0.7, and a Gaussian function was used as a radius adjustment function.

4. Results

4.1. Monthly mean temperature field

The monthly temperature of January and July averaged over a 30-year time period is given in Figures 6 and 7, respectively, for (a) observation interpolated by the objective analysis to model grid points (G_OBS), (b) uncorrected WRF simulation (U_WRF) and (c) statistically corrected simulation results (C_WRF). G_OBS is produced by the objective analysis. Thus, the spatial heterogeneities of the interested area's physiography are hardly embedded in G_OBS. As shown in Figures 6(a) and 7(a), a relatively warm temperature divides the Altai mountain ranges into two parts, as well as the Khangai mountain ranges located in the central part of Mongolia. The objectively interpolated warm temperature existing near the west southern boundary, which is obviously an unrealistic temperature, is mainly due to the simple objective analysis with sparse observational

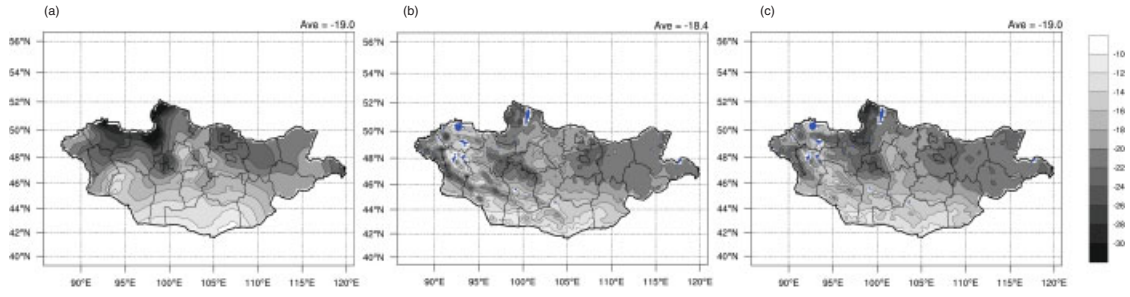

Figure 6. Monthly mean temperature distribution for January, averaged over thirty years (1981–2010): (a) gridded observation by objective analysis (G_OBS), (b) simulated by WRF (U_WRF), and (c) corrected WRF (C_WRF).

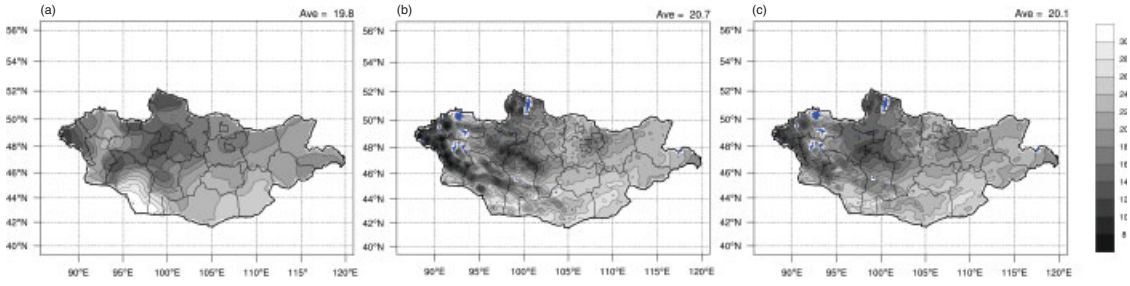

Figure 7. Monthly mean temperature distribution for July, averaged over thirty years (1981–2010): (a) gridded observation by objective analysis (G_OBS), (b) simulated by WRF (U_WRF), and (c) corrected WRF (C_WRF).

network (Figure 1). Nevertheless, the G_OBS pattern for statistical correction expressed the overall temperature distribution over Mongolia.

On the contrary, the results simulated by WRF with a horizontal resolution of 20 km expressed a more detailed pattern of temperature over the whole area of interest, especially over the mountain areas. However, the simulated results included incredulous values compared to the G_OBS pattern during both January and July. Particularly, the relative cold temperature in G_OBS near Uvs Lake, which is the biggest lake in Mongolia and is located in the northwest of Mongolia, was not simulated reasonably (Figures 6(b) and 7(b)). These shortcomings were mainly due to the systematic biases in the model.

The corrected results based on dynamical downscaling and statistical corrections are shown in Figures 6(c) and 7(c). After the statistical correction, C_WRF provided the detailed temperature distribution obtained in U_WRF, as well as the general pattern shown in G_OBS. The advantage of dynamical downscaling in which complex topography is evaluated was preserved in the monthly mean temperature of C_WRF.

Scatter plots of monthly mean temperature in July and January with respect to altitude are shown in Figures 8 and 9, respectively, for *in situ* observation, G_OBS, U_WRF and C_WRF. Figure 8 shows that G_OBS has spread variations with height unlike the *in situ* observation at different altitudes since the effect of topography is lost during the horizontal interpolation by the objective analysis. As shown in Figure 8(c), U_WRF temperature decreases with increasing height as the *in situ* observations (Figure 8(a)). However, there is a systematic warm bias between the regressed lines of the *in situ* observations and U_WRF. After application of the correction method, the bias was reduced and C_WRF temperature approached relatively close to the *in situ* observation (Figure 8(d)).

However, the results were different during winter and the lapse rate of the monthly mean temperature became negative, as shown in Figure 11(a). In U_WRF

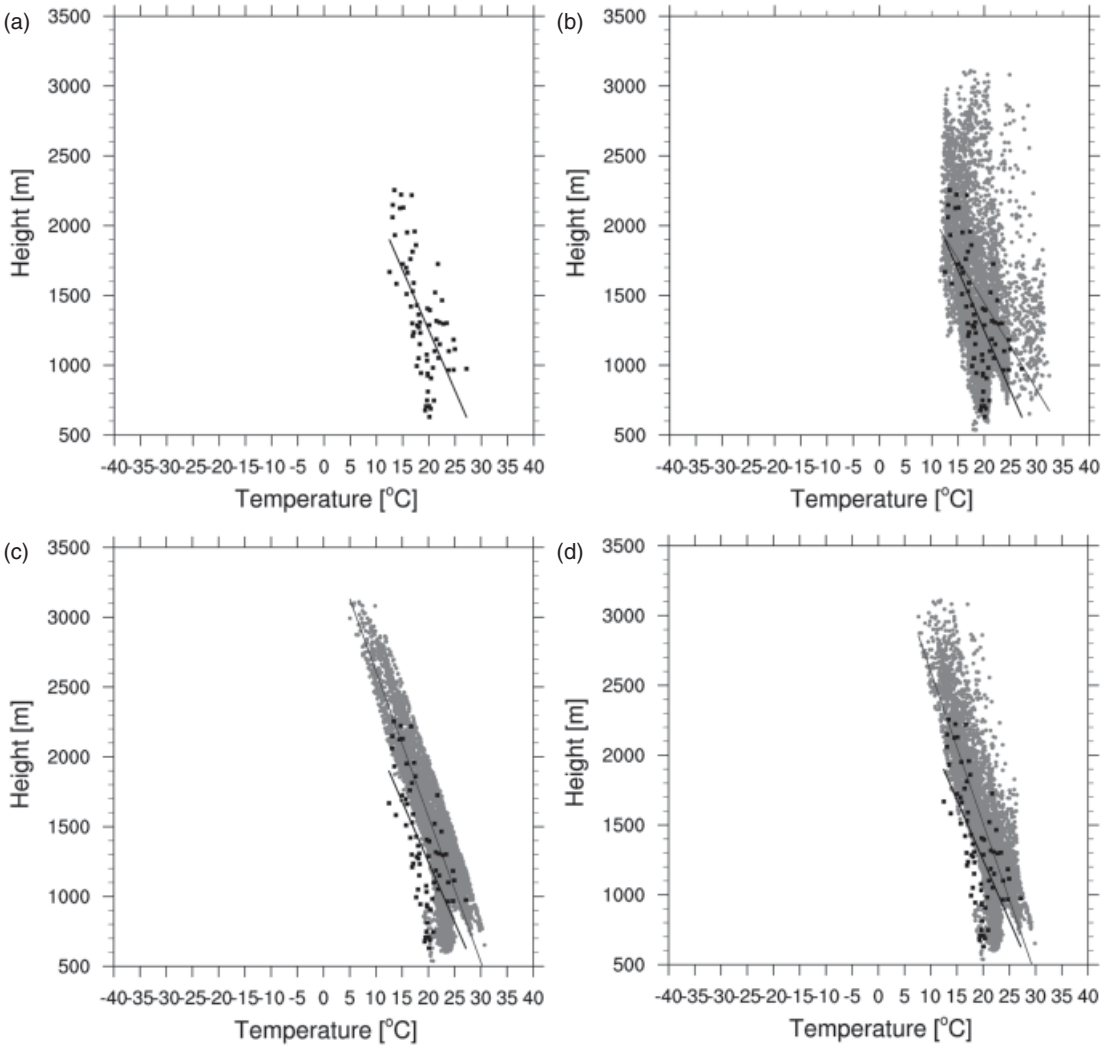

Figure 8. Scatter plots of monthly mean temperature against elevation over Mongolia for July: (a) *in situ* observation at stations, (b) G_OBS, (c) U_WRF and (d) C_WRF. Black closed rectangles and gray closed circles are observed and simulated temperature of G_OBS, U_WRF, C_WRF, respectively. Black and gray lines are regressed by least square for observation and simulation for each.

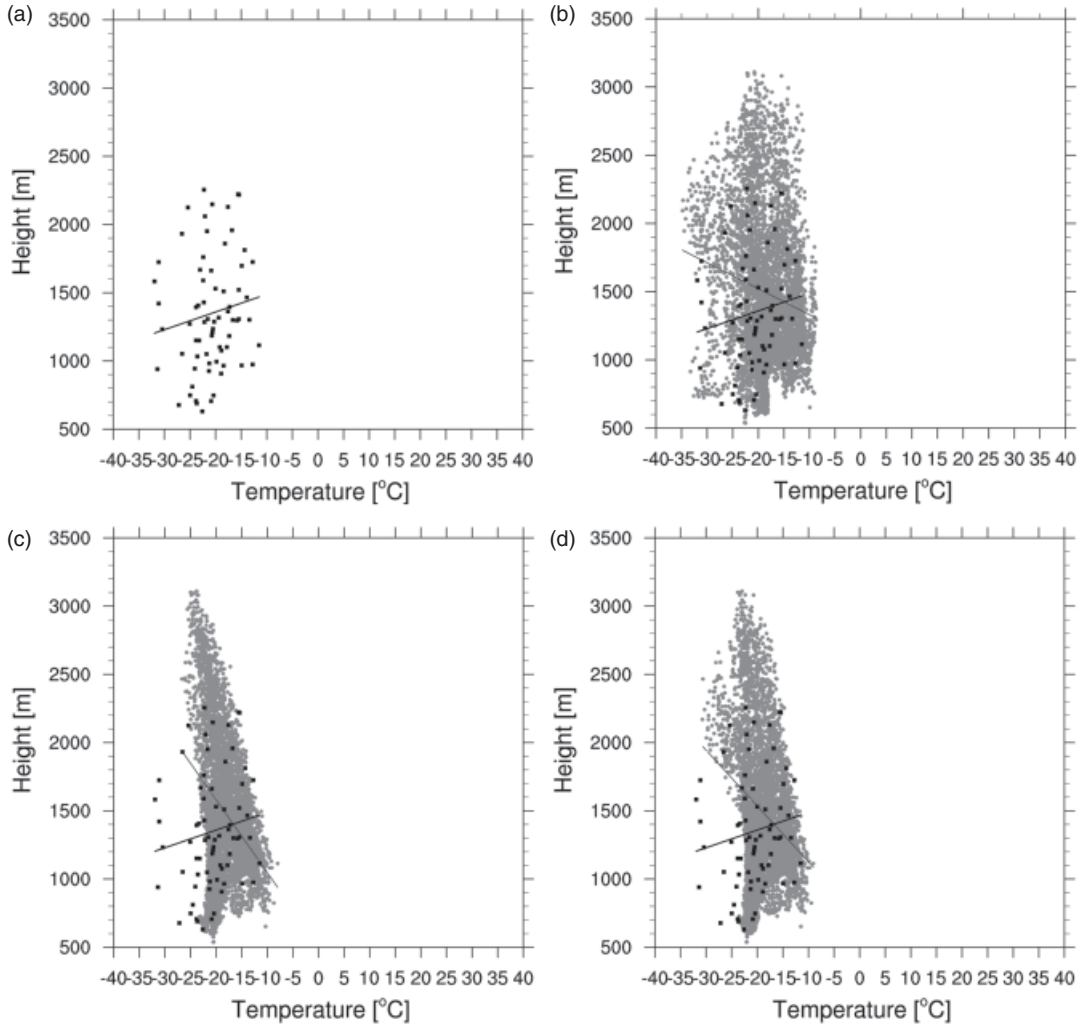

Figure 9. Scatter plots of monthly mean temperature against elevation over Mongolia for January: (a) *in situ* observation at stations, (b) G_OBS, (c) U_WRF and (d) C_WRF. Black closed rectangles and gray closed circles are observed and simulated temperature of G_OBS, U_WRF and C_WRF, respectively. Black and gray lines are regressed by least square for observation and simulation for each.

and C_WRF, however, the lapse rates were positive. This discrepancy was due to the model's insufficient simulation of the temperature inversion. The inversion correction was therefore done for the cold season and the results are presented in the next section.

4.2. The inversion corrected monthly mean temperature

Figure 9 shows that inversion correction is necessary for proper reproduction of temperature in regions with strong inversion such as Mongolia, particularly during the cold season, in addition to statistical correction.

In Figure 10, the monthly mean temperature for January is given for G_OBS, U_WRF, C_WRF results by Equation (3) and WRF results with inversion correction (IC_WRF) by Equation (6). The U_WRF and C_WRF results were much warmer than the observation within the deep inversion area, especially near Uvs Lake. However, after the inversion correction, it became colder than C_WRF and the area-averaged temperature decreased by 1.2 °C in IC_WRF.

In order to illustrate the improvement in the simulated temperature due to the inversion correction, a scatter plot of the monthly mean vertical temperature in the northwestern part of Mongolia, from 91°E to 97°E and from 48°N to 51°N, where deep inversion occurs during the cold season, is shown in Figure 11. In the figure, the vertical distribution of the monthly mean temperature in U_WRF and C_WRF was very different from the *in situ* observation at the stations. As a result of the inversion correction, the vertical distribution temperature in the low-lying selected area approached closely to the observation, as in IC_WRF. Over the weak inversion area, the distribution was already relatively close to the observation in both U_WRF and C_WRF (Figure 12).

4.3. Verification of the results with the observation

In this section, the results of U_WRF, C_WRF and IC_WRF are compared with the *in situ* observations using statistical analysis such as anomaly correlation coefficient (ACC), pattern correlation coefficient (PCC) (pattern_cor in NCL, 2012), root mean square difference

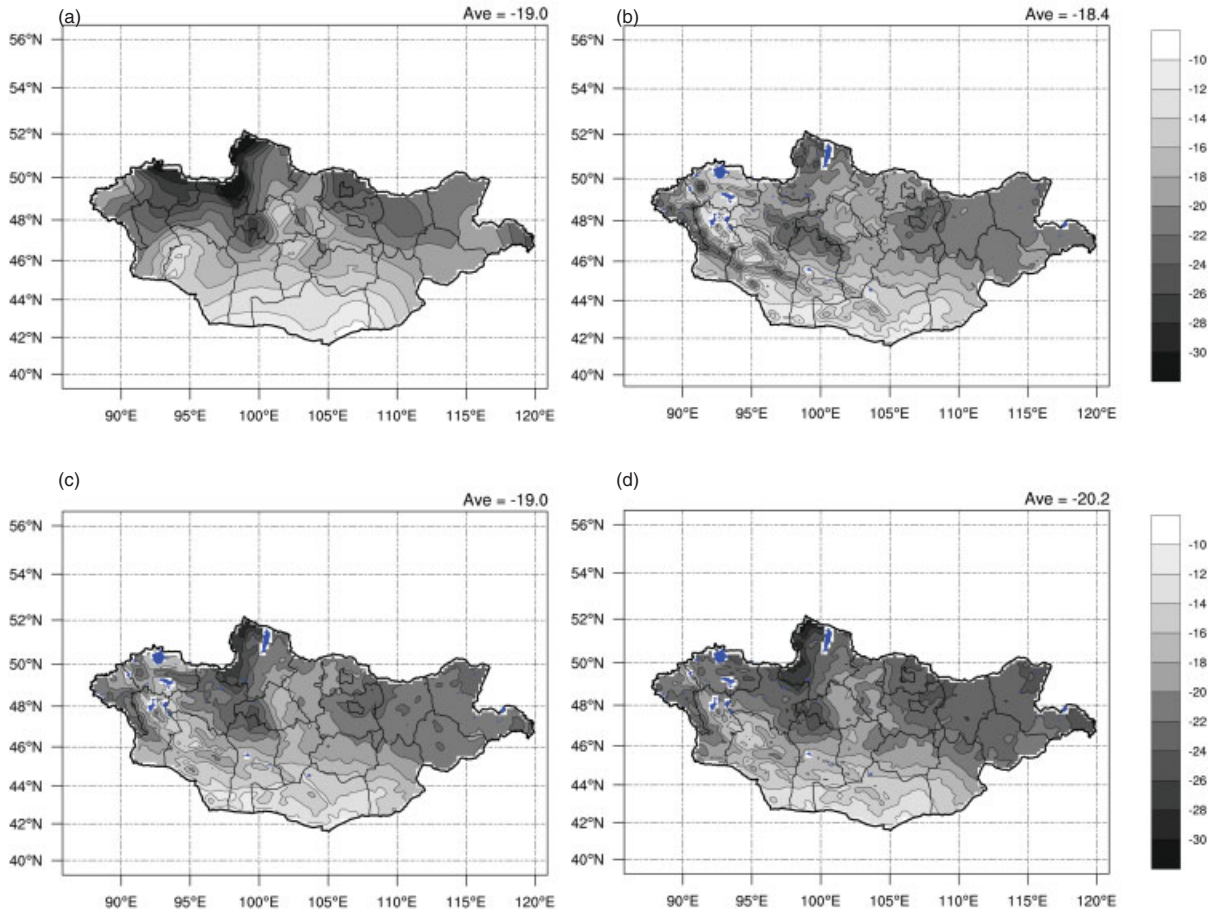

Figure 10. Monthly mean temperature distribution for January: (a) G_OBS, (b) U_WRF, (c) C_WRF and (d) inversion corrected WRF (IC_WRF).

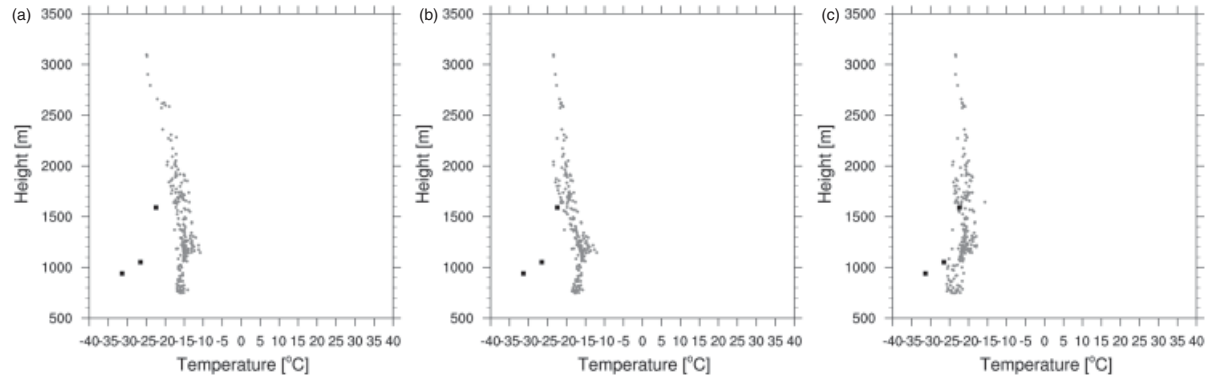

Figure 11. Scatter plots of monthly mean temperature against altitude within deepest inversion area, which covers from 48°N to 51°N and from 91°E to 97°E for January: (a) U_WRF, (b) C_WRF and (c) IC_WRF. Gray circles are model results, and black rectangles are *in situ* observations.

(RMSD), normalized standard deviation (NSTD) and a Taylor diagram (Taylor, 2001).

ACC, RMSD and NSTD are expressed as:

$$\mathrm{ACC} = \frac{\sum_{i=1}^{N} o_{ij}' f_{ij}'}{\left[\sum_{i=1}^{N} \left(o_{ij}'\right)^2 \sum_{i=1}^{N} \left(f_{ij}'\right)^2\right]^{\frac{1}{2}}} \tag{8}$$

$$\mathrm{RMSD} = \sqrt{\frac{\sum_{i=1}^{N} \left(o_{ij} - f_{ij}\right)^2}{N}} \tag{9}$$

$$NSTD = \frac{f_\sigma}{o_\sigma} \tag{10}$$

where $o_{ij}' = o_{ij} - \overline{o_j}$, $f_{ij}' = f_{ij} - \overline{f_j}$, observation ($o$) and output ($f$) of U_WRF, C_WRF and IC_WRF, respectively at each grid point. ($\overline{\ }$) and ($_\sigma$) are

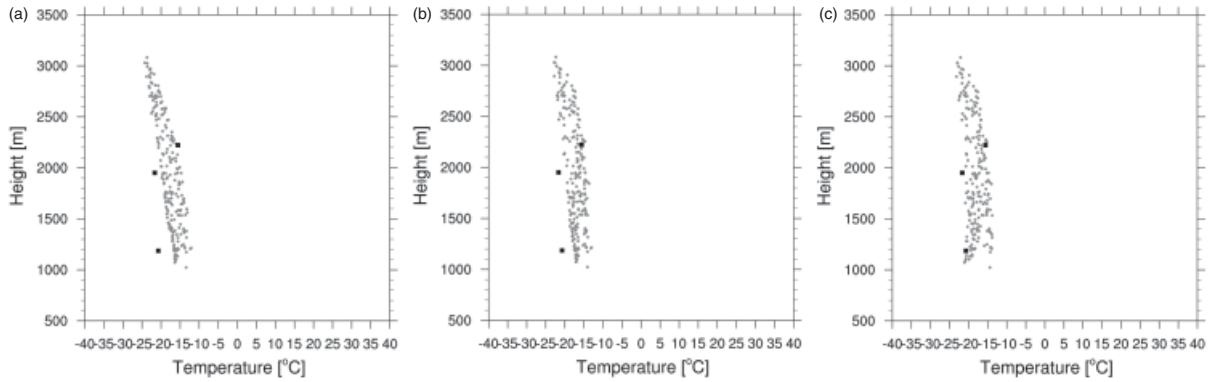

Figure 12. Scatter plots of monthly mean temperature against altitude within the weak inversion area from 45°N to 47°N and from 91°E to 95°E for January: (a) U_WRF, (b) C_WRF and (c) IC_WRF. Gray circles are model results, and black rectangles are *in situ* observations.

climatology and standard deviation, respectively, for the period 1981–2010. N and j are the number of years and grid points, respectively.

PCC-RMSD is shown in Figure 13, which comprises 30-year means for each month. The open circles and gray closed circles and the rectangles indicate U_WRF, IC_WRF and C_WRF, respectively. The model results nearest to the 70 stations (Figure 1) were compared to the observation. Throughout the whole year, except February and March, RMSD was decreased and PCC became close to 1.0 in IC_WRF. As shown in the figure, RMSD and PCC in U_WRF were high and low relative to the corrected results, respectively. In addition, RMSD and PCC of IC_WRF in the warm season were similar to C_WRF due to the absence of any inversion effect during the season in Mongolia.

Figure 14 shows a Taylor diagram representing the temporal correlation and NSTD between the two WRF results and the *in situ* observed anomalous surface air temperature. The numbers indicate months, the gray

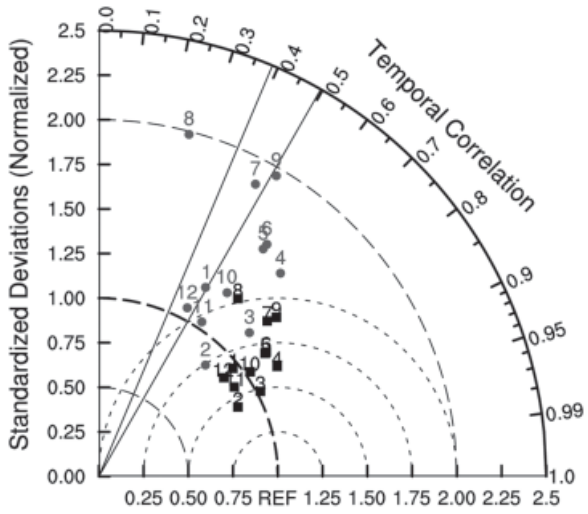

Figure 14. Taylor diagram of anomalous air temperature over Mongolia for January to December, 1981–2010. Gray and black colours are U_WRF and C_WRF, respectively.

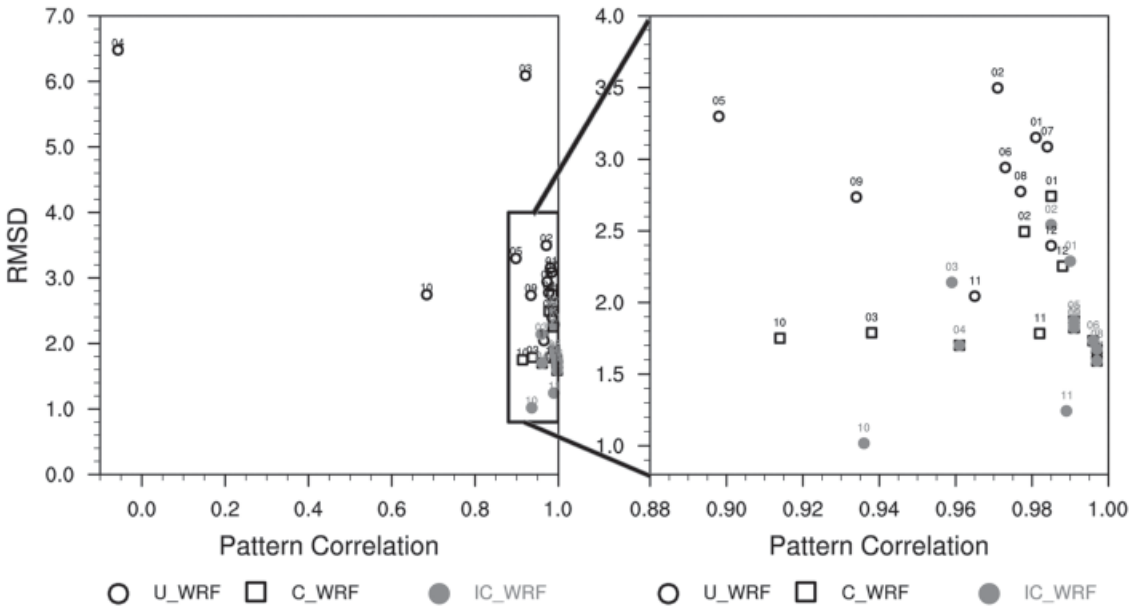

Figure 13. Pattern correlation *versus* RMSD of monthly mean temperature for U_WRF, C_WRF and IC_WRF.

Table 5. Annual mean basic statistics for the anomaly correlation coefficient (ACC), and root mean square difference (RMSD) derived from anomaly surface air temperature nearest to the stations.

	U_WRF	C_WRF
ACC	0.5	0.8
RMSD (°C)	2.0	1.0

closed circle U_WRF, and the red black C_WRF. ACC of U_WRF was below the 95% significance level for August and between 95 and 99% for January, July and December, whereas all the ACCs of C_WRF were above the 99% significance level. NSTD fell within the range of 0.8–1.3 after correction. In addition, as shown in Table 5, ACC was 0.5 in U_WRF but was improved by 0.3–0.8, while RMSD was decreased to 1.0 °C from 2.0°. Thus, the correction method used in this study was also useful for the temporal variation of the temperature anomaly.

Figure 15 shows RMSD of the monthly surface mean temperature from 1981 to 2010 in both gridded and *in situ* station points. RMSD was within 3.0–6.5 °C in U_WRF for all months but fell to 1.8–3.0 °C in C_WRF, and was further decreased by 0.3–0.4 °C after inversion correction. The monthly mean temperatures averaged over the 70 *in situ* stations (Figure 1) are given in Table 6. The U_WRF, C_WRF and IC_WRF temperatures in the table are the values averaged over the 70 grid points, each of which is nearest from each *in situ* observation site. U_WRF had a warm bias in January and December, but a cold bias during February to May. In general, the U_WRF result showed a cold bias in Mongolia. However, after statistical correction in C_WRF, the annual mean temperature increased to 1.8 °C from −1.2 °C. After inversion correction, the annual mean temperature became 0.9 °C.

5. Discussion and conclusions

A fine spatial temperature distribution over Mongolia, which cannot be obtained by sparsely distributed observational data due to the country's complex topography, is presented in this study using dynamical downscaling and statistical correction with consideration for the atmospheric inversion effect. The gridded temperature pattern objectively analyzed by 70 meteorological stations did not contain the physiographical characteristics and heterogeneities of the area of interest.

On the contrary, the result from the relatively fine-resolution WRF model presented a detailed structure of temperature such as terrain-following features since the model considered the topographical effect. In order to reproduce the air temperature distribution for Mongolia, WRF was performed from 1981 to 2010, using NCEP/NCAR reanalysis II data as the initial and boundary conditions. A statistical correction was applied taking advantage of the WRF model in order to remove the systematic bias of the model.

In order to remove the systematic biases in the model, statistical correction was applied for both mean and perturbation parts. For correction of the mean part, both the inversion effect and the mean model bias were considered in the correction. As the temperature inversion simulated by the model was much weaker than the observation derived from radiosonde data, temperature inversion was considered in the correction. For the perturbation correction, SOM, an ANN technique developed, was used.

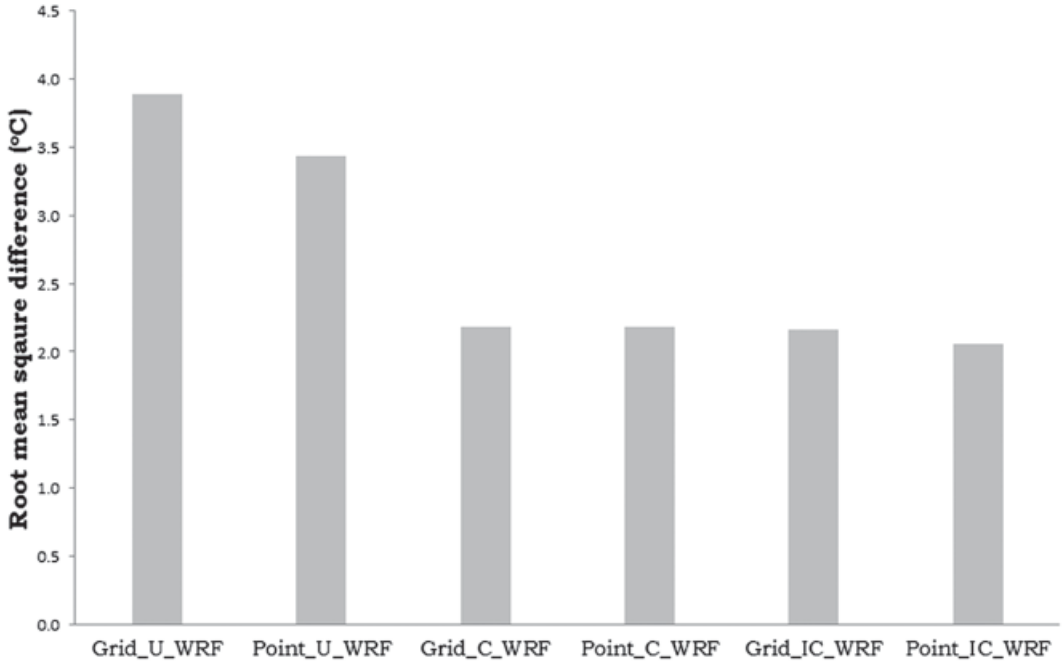

Figure 15. RMSD of annual mean temperature for 30 years (1981–2010) in gridded (Grid) and station point (Point).

Table 6. Summary of the monthly mean temperatures averaged over 70 stations.

	January	February	March	April	May	June
Obs	−20.8	−16.5	−7.5	3.1	11.0	16.5
U_WRF	−19.1	−17.9	−13.1	−3.3	8.3	16.4
C_WRF	−19.1	−14.8	−6.1	4.3	12.3	17.8
IC_WRF	−20.6	−17.5	−8.2	4.3	12.3	17.8

	July	August	September	October	November	December
Obs	18.8	16.6	10.2	1.4	−9.6	−17.7
U_WRF	20.0	16.7	9.6	1.0	−9.9	−16.9
C_WRF	20.1	17.9	11.5	2.7	−8.3	−16.3
IC_WRF	20.1	17.9	11.5	1.4	−10.0	−17.8

The study results revealed that the statistical and inversion correction methods used are applicable when there is strong inversion at the atmospheric surface layer. After the corrections, the pattern correlations between the models and the *in situ* observation were increased, and RMSD decreased, indicating the effectiveness of the developed correction methods. In addition, the temporal ACC was also increased after the application of the statistical correction. These results imply that our correction method improves not only spatial patterns with fine resolution but also the time-varying temperature variance over Mongolia. The study methodology's successful reproduction of gridded climate information with a fine-scale that reflected the local climate characteristics over Mongolia demonstrated its potential advantage in overcoming any deficiency in or paucity of ground-based observation.

Acknowledgements

This work was carried out with the support of Korea Meteorological Administration Research and Development Program under Grant CATER 2012–3083 and Rural Development Administration Cooperative Research Program for Agriculture Science and Technology Development under Grant Project No. PJ009353, Republic of Korea.

References

Ahn JB, Park CK, Im ES. 2002. Reproduction of regional scale surface air temperature by estimating systematic bias of mesoscale numerical model. *J. Korean Meteorol. Soc.* **38**(1): 69–80.

Ahn JB, Lee J, Im ES. 2012. The reproducibility of surface air temperature over South Korea using dynamical downscaling and statistical correction. *J. Meteor. Soc. Jpn.* **90**(4): 493–507.

Altangerel B, Sato T, Ishikawa M, Tsogt J. 2011. Performance of dynamical downscaling for extreme weather event in Eastern Mongolia: case study of severe windstorm on 26 May 2008. *Sola* **7**: 117–120.

Amengual A, Homar V, Romero R, Alonso S, Ramis C. 2012. A statistical adjustment of regional climate model outputs to local scales: application to Platja de Palma, Spain. *J. Climate* **25**: 939–957, DOI: 10.1175/JCLI-D-10-05024.1.

Conway D, Wilby RL, Jones PD. 1996. Precipitation and air flow indices over the British Isles. *Climate Res*. **7**: 169–183.

Coulibaly P, Dibike YB, Anctil F. 2005. Downscaling Precipitation and Temperature with Temporal Neural Networks. *J. Hyd.* **6**: 483–496.

Cressman GP. 1960. An operational objective analysis system. *Mon. Weather Rev.* **87**(10): 367–374.

Déqué M, Rowell DP, Lüthi D, Giorgi F, Christensen JH, Rockel B, Jacob D, Kjellström E, de Castro M, van den Hurk B. 2007. An intercomparison of regional climate simulations for Europe: assessing uncertainties in model projections. *Clim. Change* **81**: 53–70.

Dudhia J. 1989. Numerical study of convection observed during the winter monsoon experiment using a mesoscale two-dimensional model. *J. Atmos. Sci.* **46**: 3077–3107.

Ek MB, Mitchell KE, Lin Y, Rogers E, Grunmann P, Koren V, Gayno G, Tarpley JD. 2003. Implementation of Noah land surface model advances in the National Centers for Environmental Prediction operational mesoscale Eta model. *J. Geophys. Res.* **108**: 8851, DOI: 10.1029/2002JD003296.

Erdenesukh S. 2008. Studies on inversion near ground surface layer in Mongolia. *Ph.D. dissertation. Nat'l.Univ. Mongolia*, 2273.

Fischer EM, Schär C. 2010. Consistent geographical patterns of changes in high-impact European heatwaves. *Nat. Geosci.* **3**(6): 398–403, DOI: 10.1038/ngeo866.

Gomboluudev P, Oyunjargal L, Batbold A, Natsagdorj L. 2005. Mesoscale numerical case study and analysis of cyclone development. *Proceeding of the First Symposium on Terrestrial change in Mongolia*. Ulaanbaatar.

Henrik F, Navarra A, Ward MN. 1999. Reduction of model systematic error by statistical correction for dynamical seasonal predictions. *J. Climate* **12**: 1974–1989.

Hong S-Y, Lim J-OJ. 2006. The WRF single-moment 6-class microphysics scheme (WSM6). *J. Korean Meteorol. Soc.* **42**: 129–151.

Hong S-Y, Noh Y, Dudhia J. 2006. A new vertical diffusion package with an explicit treatment of entrainment processes. *Mon. Wea. Rev*. **134**: 2318–2341.

Im ES, Ahn JB, Remedio AR, Kwon WT. 2008. Sensitive of the regional climate of East/Southeast Asia to convective parameterizations in the RegCM3 modeling system. Part1: focus on the Korean peninsula. *Int. J. Climatol.* **28**: 1861–1877.

Kain JS. 2004. The Kain-Fritsch convective parameterization: an update. *J. Appl. Meteorol.* **43**: 170–181.

Kohonen T. 1990. The self-organizing maps. *Proc. IEEE* **78**: 1464–1480.

Lorenz EN. 1963. Deterministic nonperiodic flow. *J. Atmos. Sci.* **20**: 130–148.

Meehl GA. 1995. Global coupled general circulation models. *Bull. Am. Meteorol. Soc.* **76**: 951–957.

Mlawer EJ, Taubman SJ, Brown PD, Iacono MJ, Clough SA. 1997. Radiative transfer for inhomogeneous atmospheres: RRTM: a validated correlated-k model for the longwave. *J. Geophys. Res.* **102**(D14): 16663–16682.

NCL. 2012. The NCAR Command Language (Version 6.1.0) [Software]. UCAR/NCAR/CISL/VETS: Boulder, Colorado. DOI: 10.5065/-D6WD3XH5.

Schoof JT, Pryor SC. 2001. Downscaling temperature and precipitation: a comparison of regression-based methods and artificial neural networks. *Int. J. Climatol.* **21**: 773–790.

Sun J, Chen H. 2012. A statistical downscaling scheme to improve global precipitation forecasting. *Meteorol. Atmos. Phys.* **117**: 87–102, DOI: 10.1007/s00703-012-0195-7.

Taylor KE. 2001. Summarizing multiple aspects of model performance in a single diagram. *JGR* **106**(D7): 7183–7192.

Wilks DS. 1995. *Statistical Methods in the Atmospheric Sciences*. Academic Press: New York, NY.

Wood AW, Leung LR, Sridhar V, Lettenmaier DP. 2004. Hydrologic implications of dynamical and statistical approaches to downscaling climate model outputs. *Clim. Change* **62**: 189–216.

Xu CY. 1999. From GCM to river flow: a review of downscaling methods and hydrologic modeling approaches. *Prog. Phys. Geogr.* **23**: 229–249.